

# Coupling of electronic transition to ferroelectric order in a 2D semiconductor

Received: 30 September 2024

Accepted: 8 February 2025

Published online: 23 February 2025

 Check for updates

Chun-Ying Huang <sup>1,7</sup>, Daniel G. Chica<sup>1,7</sup>, Zhi-Hao Cui <sup>1,7</sup>, Taketo Handa <sup>1</sup>, Morgan Thinel <sup>1,2</sup>, Nicholas Olsen <sup>1</sup>, Yufeng Liu<sup>1</sup>, Michael E. Ziebel <sup>1</sup>, Guiying He <sup>3,4</sup>, Yinming Shao <sup>2,5</sup>, Connor A. Occhialini<sup>2,6</sup>, Jonathan Pellicciari <sup>6</sup>, Dmitri N. Basov <sup>2</sup>, Matthew Sfeir <sup>3,4</sup>, Abhay Pasupathy <sup>2</sup>, Valentina Bisogni <sup>6</sup>, David R. Reichman <sup>1</sup> ✉, Xavier Roy <sup>1</sup> ✉ & Xiaoyang Zhu <sup>1</sup> ✉

A ferroelectric material often exhibits a soft transverse optical (TO) phonon mode which governs its phase transition. Charge coupling to this ferroelectric soft mode may further mediate emergent physical properties, including superconductivity and defect tolerance in semiconductors. However, direct experimental evidence for such coupling is scarce. Here we show that a photogenerated coherent phonon couples strongly to the electronic transition above the bandgap in the van der Waals (vdW) two-dimensional (2D) ferroelectric semiconductor NbOI<sub>2</sub>. Using terahertz time-domain spectroscopy and first-principles calculations, we identify this mode as the TO phonon responsible for ferroelectric order. This exclusive coupling occurs only with the above-gap electronic transition and is absent in the valence band as revealed by resonant inelastic X-ray scattering. Our findings suggest a new role of the soft TO phonon mode in electronic and optical properties of ferroelectric semiconductors.

In conventional polar semiconductors where lattice displacements are described by harmonic oscillators, the coupling between charge carriers and nuclei is dominated by longitudinal optical (LO) phonons. This is the so-called Fröhlich interaction which describes the long-range interaction between a charge carrier and the effective dipoles along the LO phonon coordinate<sup>1,2</sup>. By contrast, the Coulomb interactions of transverse optical (TO) phonon mode have a negligible contribution to the long wavelength electric field due to the lack of macroscopic polarization. However, in ferroelectric and paraelectric materials, the unique TO phonon mode is characterized by a double-well potential with minima at two non-zero electric polarizations of equal magnitudes but opposite signs<sup>3,4</sup>. Such a TO mode is typically labeled as “soft” as the double well flattens, and the corresponding

frequency decreases with increasing temperature towards the phase transition. The presence of electric polarizations in the double well can lead to new carrier-TO phonon interactions beyond the Fröhlich model. Wemple et al.<sup>5</sup> pioneered the idea that scattering of carriers with polar nano-domains formed from fluctuating polarization in the double well-determined carrier mobility in oxide perovskites. These types of carrier interactions with soft TO phonons have been invoked in other related models and in computational studies<sup>5–9</sup>. Zhu and coworkers proposed the ferroelectric polaron model to explain the defect tolerance and long carrier lifetimes in a class of paraelectric semiconductors, lead halide perovskites (LHPs)<sup>10–13</sup>. In this model, Coulomb interactions of charge carriers are efficiently screened by induced and/or pre-formed polar nano-orders dictated by the soft TO

<sup>1</sup>Department of Chemistry, Columbia University, New York, NY, USA. <sup>2</sup>Department of Physics, Columbia University, New York, NY, USA. <sup>3</sup>Department of Physics, Graduate Center, City University of New York, New York, NY, USA. <sup>4</sup>Photonics Initiative, Advanced Science Research Center, City University of New York, New York, NY, USA. <sup>5</sup>Department of Physics, Pennsylvania State University, University Park, PA, USA. <sup>6</sup>National Synchrotron Light Source II, Brookhaven National Laboratory, Upton, NY, USA. <sup>7</sup>These authors contributed equally: Chun-Ying Huang, Daniel G. Chica, Zhi-Hao Cui. ✉ e-mail: [drr2103@columbia.edu](mailto:drr2103@columbia.edu); [xr2114@columbia.edu](mailto:xr2114@columbia.edu); [xyzhu@columbia.edu](mailto:xyzhu@columbia.edu)

phonon, thus drastically reducing charge carrier recombination or scattering with charged defects. The efficient screening is believed to be responsible in part for the remarkable optoelectronic properties of LHPs and other displacive paraelectric semiconductors<sup>10–14</sup>. The strong interaction between charge carriers and the soft TO mode is also believed to be responsible for charge pairing in a class of ferroelectric superconductors<sup>15,16</sup>.

Despite the significance of carrier-TO phonon coupling to charge carrier transport in ferro- and paraelectric materials, our current understanding is primarily based on conceptual models, computations, and indirect experimental evidence<sup>5–12,14,17</sup>. Here, we investigate the coupling of phonons to the electronic transition in the 2D vdW ferroelectric semiconductor NbOI<sub>2</sub>, which exhibits in-plane ferroelectric polarization and an optical bandgap in the visible range<sup>18,19</sup>. The vdW nature of NbOI<sub>2</sub> leads to little interlayer interaction<sup>20</sup>, thus allowing us to probe the interactions primarily in 2D, in which Coulomb interaction is strong. Using pump-probe coherent phonon spectroscopy, we find that the electronic transition above the bandgap couples exclusively to a phonon mode at 3.1 THz, which is identified as the TO phonon in terahertz time-domain spectroscopy (THz-TDS). Theoretical modeling based on density functional theory (DFT) reveals that this TO phonon mode corresponds to the stretching of the Nb–O polar bonds responsible for ferroelectric order. Using resonant inelastic X-ray scattering (RIXS) spectroscopy<sup>21–23</sup>, we further establish that the ferroelectric TO mode couples exclusively with the electronic transition above the bandgap, a mechanism distinct from valence-band electron-phonon coupling.

## Results and discussions

We grow millimeter-size single crystal NbOI<sub>2</sub> with optically flat surfaces (Supplementary Fig. 1), using the chemical vapor transport method<sup>18</sup> and confirm the phase purity through powder X-ray diffraction (Supplementary Fig. 1b). NbOI<sub>2</sub> adopts a vdW layered monoclinic crystal structure in the *C2* space group (Fig. 1a, b). Along the *b*-axis, the Nb atoms are displaced from the center position, resulting in unequal Nb–O bond lengths and spontaneous polarization along the *b*-axis. Scanning tunneling microscopy (STM) image (Fig. 1c) of the crystal surface freshly cleaved in vacuum confirms the rectangular in-plane structure with lattice parameters consistent with those obtained by single-crystal X-ray diffraction (Supplementary Fig. 2). The anisotropic in-plane crystal structure gives rise to an anisotropic electronic structure, as revealed by differential reflectance ( $\Delta R/R$ ) spectroscopy (Fig. 1d). The  $\Delta R/R$  spectrum along the *c*-axis reveals above-gap transitions at 2.3 eV and 2.6 eV<sup>18</sup>; these transitions are absent along the *b*-axis. A weak onset in absorption is visible at ~1.1 eV (Supplementary Fig. 3), likely due to an indirect optical transition. By performing high-temperature second harmonic generation (SHG) and Raman spectroscopy, we also find the ferroelectric phase remains robust up to 573 K (Supplementary Fig. 4).

To determine the phonon modes in NbOI<sub>2</sub>, we performed polarization-angle resolved Raman spectroscopy with incident polarization in the *bc* (*yz*) plane and scattered polarization parallel (pp) or perpendicular (cp) to incident polarization. The polarization angle ( $\theta^\circ$ ) is referenced to the crystallographic *c*-axis. Fig. 2a, b present pseudocolor plots of Raman spectra with pp and cp polarizations, respectively, along with polar plots of the Raman peak intensities for the strongest mode at  $3.137 \pm 0.002$  THz ( $104.5 \text{ cm}^{-1}$ , labeled as P2 in main text) in Fig. 2c. This mode is highly anisotropic and preferentially allowed along the *b*-axis for pp (red). For cross-polarization (blue), the polar plot is symmetric along the diagonals between the *b*- and *c*-axes. We conduct Raman tensor analysis to assign symmetries to the Raman-active phonons (see Supplementary Notes and Supplementary Fig. 5 for details)<sup>24–27</sup>. We extract line-cuts of the spectra at  $\theta = 0^\circ$  (*c*-axis) and  $90^\circ$  (*b*-axis) to show the anisotropy of the Raman-active modes (Fig. 2d). A comparison of the experimental data with theoretical

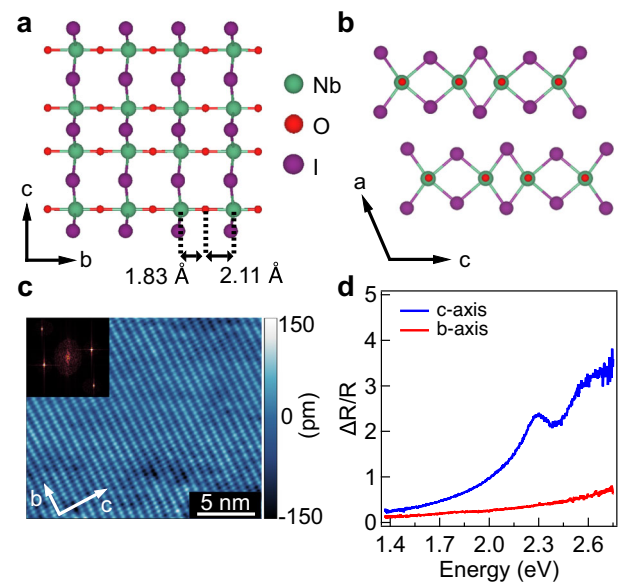


**Fig. 1 | Structure and optical transitions in NbOI<sub>2</sub>.** **a, b** Crystal structure of NbOI<sub>2</sub> viewed perpendicular to *bc*-plane (**a**) and along *b*-axis (**b**). **c** Scanning tunneling microscopy image of cleaved NbOI<sub>2</sub> single crystal at room temperature (RT). The inset shows the FT of the topography. **d** Differential reflectance spectra of 7-layer NbOI<sub>2</sub> on z-cut quartz with incident light polarized along either crystallographic *c*- or *b*-axis at RT.  $\Delta R$  is defined as  $R_{\text{sample}} - R_{\text{substrate}}$  in steady state and  $R$  in the denominator is  $R_{\text{substrate}}$ .

Raman spectra calculated from first-principles DFT in Fig. 2e shows good agreement across the measured range (see Methods and Supplementary Table 1 for full assignment of calculated Raman modes). In particular, an excellent agreement can be confirmed for the anisotropy of the main phonon mode (this mode is 2.83 THz in computation, corresponding to the P2 mode in experiments), as shown in Fig. 2f. The discrepancy in the position of the small shoulder peak—down-shifted in the experiment (the P1 mode) and up-shifted in simulation—may be attributed to anharmonicity. While anharmonicity is experimentally evidenced by the temperature dependence of its full-width-at-half-maximum (FWHM) and center-frequency shift, Supplementary Fig. 4c and d, respectively, it is very challenging to include anharmonicity in computation<sup>28</sup>. Such computational effort is beyond the scope of the current study and may be of interest for the future<sup>28</sup>. As detailed below, the main phonon mode, P2, corresponds to the ferroelectric TO phonon and strongly couples to photogenerated carriers.

We carry out ultrafast pump-probe coherent phonon spectroscopy (CPS) to probe how the electronic transition couples to phonons in NbOI<sub>2</sub>. We use an excitation laser pulse (pulse width ~150 fs) centered at  $h\nu_1 = 2.58$  eV, which is resonant with the second above-gap transition, with light incidence normal to the surface and polarization parallel to the *c*-axis. Fig. 3a and b show the transient reflectivity spectrum ( $\Delta R/R_0$ , where  $R_0$  is reflectance without the pump and  $\Delta R$  is the pump-induced change in reflectance), probed by a broadband pulse ( $h\nu_2 = 1.46 - 2.50$  eV) polarized parallel to the *c*- or *b*-axis, respectively. In transient reflectance probed along the optical-transition allowed direction (*c*-axis), there is a clear signature of exciton bleaching at ~2.20–2.35 eV, with periodic modulation of the signal arising from coherent phonon(s). The clear oscillatory signals at delay times > 30 ps without subtracting the electronic signal demonstrate the long coherence time at room temperature with a decay constant of ~30 ps (also see Supplementary Fig. 6 for short-time Fourier transform analysis and fitting of the dephasing time). The full kinetic trace of exciton bleaching (Supplementary Fig. 7) can be described by a long decay time constant of  $\tau_d = 5.6 \pm 1.2$  ns. After the removal of the incoherent decay component, the Fourier transform (FT) of the residue

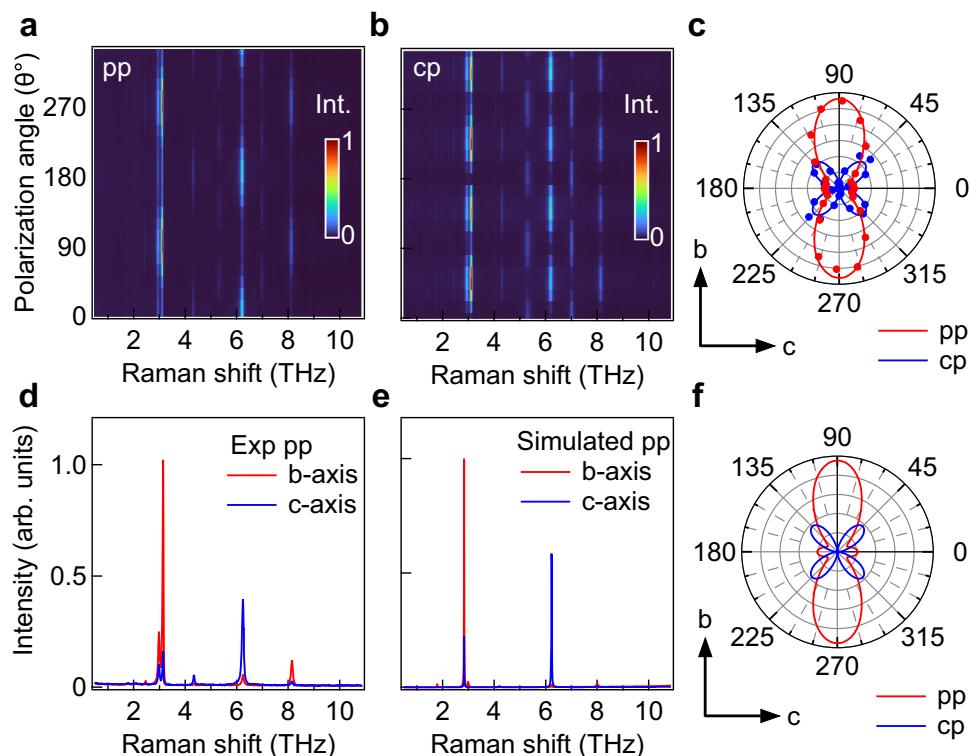


**Fig. 2 | Polarization-angle resolved Raman Spectra and Symmetry Analysis.**

**a, b** Polarization-angle resolved Raman spectra of  $\text{NbOI}_2$  at RT with incident polarization in the  $yz$  plane ( $y = b$ -axis,  $z = c$ -axis) and scattering polarization parallel (a) or perpendicular (b) to incident polarization. 0 degree is referenced to the crystallographic  $c$ -axis. The color bar represents the Raman scattering intensity (normalized to the highest intensity for clarity). pp represents parallel polarization and cp represents cross polarization. **c** Polar plot corresponding to spectral cut from (a) and (b) at 3.137 THz mode (P2 mode). Solid lines are fitting curves obtained

by the global fit to both pp and cp data with Supplementary Equations 1 and 2 in Supplementary Text, respectively. **d** Parallel polarized Raman spectrum with incident polarization aligned to either the  $b$  or  $c$ -axis. **e** Simulated Raman spectra at 300 K with parallel polarization. **f** Simulated polar plot of the phonon mode at a calculated frequency of 2.830 THz. An empirical term,  $\cos \varphi_{c-b}$ , that was deduced from the experimental P2 mode data and describing the phase difference between two tensor elements was applied to the simulation to account for the finite absorption of incident light.

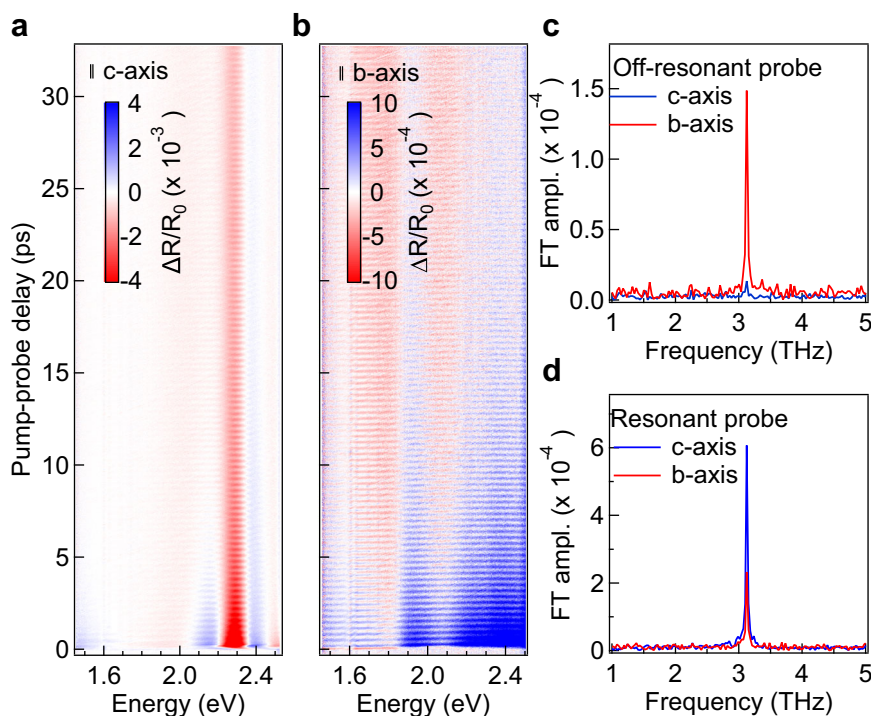


**Fig. 3 | Coherent Phonon Spectra Reveal the Dominant TO mode.** **a, b** Transient reflectivity spectra of  $\text{NbOI}_2$  measured at RT for probe polarization parallel to  $c$ - (a) or  $b$ -axis (b). The color bar indicates the magnitude of  $\Delta R/R_0$ . **c** FT of the oscillatory

components extracted from (a, b) at off-resonant probe region (1.55 eV). **d** FT of the oscillator components extracted from (a, b) at resonant probe region (2.30 eV).

coherent signals (Fig. 3c and d) gives a single frequency centered at  $3.125 \pm 0.001$  THz with a FWHM of  $0.038 \pm 0.001$  THz (Supplementary Fig. 6). This oscillatory frequency closely matches the frequency of the P2 phonon mode observed in polarization-angle resolved Raman spectra.

The polarization dependencies of the CPS spectra for resonant and off-resonant probes show key differences. When probed with photon energy below the excitonic transition (off-resonant, Fig. 3c), the phonon mode dependence is highly anisotropic. The FT amplitude of the 3.125 THz peak is prominent with probe polarization along the *b*-axis ( $I_b$ ) and more than one order of magnitude lower with polarization along the *c*-axis ( $I_c$ ). The ratio  $I_c/I_b = 0.1$  from CPS data (Fig. 3c) is close to the ratio  $I_c/I_b = 0.16$  obtained from Raman spectroscopy (Fig. 2c), consistent with the symmetry of the Raman tensor. Moreover, the FWHMs of the peaks measured by CPS ( $0.038 \pm 0.001$  THz,) and Raman spectroscopy ( $0.039 \pm 0.002$  THz) are essentially the same. We conclude that with a non-resonant, below-gap probe, the P2 phonon mode revealed in CPS is determined by the same Raman tensor<sup>29,30</sup> as in conventional Raman spectroscopy.

By contrast, when we use a resonant probe (Fig. 3d), the CPS spectrum reveals the breaking of the selection rule dictated by the Raman tensor. The weak coherent phonon amplitude for probe polarization along the *c*-axis becomes dominant with the resonant probe. The FT amplitude ratio  $I_c/I_b$  for the P2 mode increases from ~0.1 with the off-resonant probe to 2.6 with the resonant probe. We attribute the emergence of the intense symmetry-forbidden P2 mode to the strong coupling between the P2 mode and the above-gap electronic transition. This coupling can result from the displacement along the P2 phonon coordinate in the potential energy surface corresponding to the optical transition due to the strong electron-phonon coupling associated with the conduction band. Since the above-gap electronic transition is related to carrier generation, this strong coupling suggests the polaronic feature of the photoexcited carriers<sup>31,32</sup>. As we show below, the P2 mode is identified as a TO phonon mode.

To reveal the nature of the P2 phonon mode, we performed terahertz time-domain spectroscopy (THz-TDS) measurements in transmission geometry on a free-standing NbO<sub>2</sub> crystal with thickness ~2.6 μm (Supplementary Fig. 8). Because the transverse nature of electromagnetic wave only allows excitation of TO phonon modes, THz-TDS directly probes TO phonons. Fig. 4a and b show the time-domain waveforms and their corresponding FT spectra along the *b*- (red) and *c*- (blue) crystallographic axes, respectively. A full spectrum of THz absorption in frequency domain is shown in Supplementary Fig. 9. The strong THz absorption peak is observed at  $3.130 \pm 0.008$  THz (Fig. 4b), and this frequency is the same as that of the exclusive mode observed in CPS (reproduced in Fig. 4c), and the main phonon peak observed in Raman spectra (the P2 mode, reproduced in Fig. 4d). These experiments confirm the TO nature of the P2 phonon mode. Therefore, we establish that the P2 TO mode is the only phonon mode that couples to the electronic transition, whereas no contribution from LO phonons is found. The absence of the commonly observed electron-LO-phonon coupling points to the uniqueness of a ferroelectric semiconductor.

To support our interpretation of experimental results, we theoretically model the phonon dispersion using DFT (Fig. 4e) and reveal the atomic motions that underlie the TO phonon mode (Fig. 4f). By computing the inner product of eigenvectors and phonon momentum, we can estimate the TO and LO character of each phonon mode at different momentum vector  $\mathbf{q}$  in the phonon dispersion. Here, we define an inner product value of 0 as a full TO character, while a value of unity is defined as a full LO character. Along the  $\Gamma$ -A direction (perpendicular to the *bc* plane and parallel to the  $\mathbf{q}$  adopted in all the optical experiments), the 2.830 THz phonon mode (3.130 THz from THz-TDs) is essentially purely TO near the zone center  $\Gamma$ , corroborating our THz-TDS results that indicate strong TO character of the P2

phonon mode. The same mode (2.830 THz along  $\Gamma$ -A in DFT) becomes highly longitudinal along the  $\Gamma$ -Y direction (parallel to the *b*-axis), and shifts to 3.128 THz (Supplementary Fig. 10 shows a clear track of the P2 mode near the  $\Gamma$  point). The discontinuity of frequency around the zone center, with the LO mode shifting to a higher frequency, is a signature of a polar phonon<sup>33</sup>. The TO-LO splitting at the zone center is ~1.21 meV in our calculations, manifesting the polar nature of this phonon mode along the direction associated with ferroelectric order.

Figure 4f shows the eigenvectors of the TO phonon mode. From both top and side views, we identify Nb and O atoms oscillating in-phase with different amplitudes, resulting in stretching and contraction of adjacent Nb-O-Nb bonds along the crystallographic *b*-axis and modulation of the local polarization. The calculated atomic motions are reminiscent of soft modes associated with displacive-type ferroelectrics; these soft modes are typically anharmonic along the direction associated with ferroelectric order. Although our calculations are based on the harmonic approximation, we expect anharmonicity in the TO phonon potential well due to its ferroelectric character. The asymmetric potential well, as a result of this anharmonicity of the TO phonon will induce a nonvanishing change in the local polarization of the material when the phonon propagates. Such local polarization fluctuations can couple to the electronic transition and modulate the band energies near the lowest direct transition as manifested in our CPS results shown above.

To further support the distinct nature of the coupling of the P2 TO mode to the electronic transition, we performed resonant inelastic X-ray scattering (RIXS) measurements<sup>21-23</sup> at the O-K edge (1s → 2p transition), Fig. 5. RIXS process here first excites a core electron, leaving a hole in the core level. This empty core is immediately filled by a valence electron with the emission of an X-ray photon which inelastically scatters phonons in the system. As such, RIXS probes electron-phonon coupling associated with the valence band, and this coupling is expected to be distinctly different from that between electronic transition and the ferroelectric TO mode. Using linearly polarized incident photons parallel to the *b*-axis ( $\pi$ -polarization) and to the *c*-axis ( $\sigma$ -polarization), we find an anisotropic response in the X-ray Absorption Spectroscopy (XAS) pre-edge (Fig. 5b) and in the high energy loss region (> 2 eV) of the RIXS spectra (Fig. 5a). This anisotropic behavior is consistent with the differential reflectance spectra in Fig. 1c, and we associate it with the anisotropic electronic structure of NbO<sub>2</sub>. In particular, the anisotropic hybridization between O 2p and Nb 4d orbitals<sup>34-37</sup> is revealed by the strong anisotropic XAS feature around 530 - 535 eV<sup>38</sup>. In the low energy loss (< 50 meV) regime of the RIXS spectrum, several spectral components overlap in the vicinity of the elastic line and are visible with both  $\sigma$  and  $\pi$  polarization. When fitting the data (Fig. 5c), we observe a resolution-limited mode at 7 meV, together with its second-order harmonic at 14 meV, and its anti-Stokes counterpart at -7 meV. The 7 meV mode matches a phonon observed with THz spectroscopy (Supplementary Fig. 9) at 1.78 THz. The intensity ratio between the 7 and 14 meV modes and the evolution of their intensity as a function of incident photon energy supports our assignment of the second peak as the higher harmonic<sup>35,37</sup>. The presence of higher-order phonon harmonics in the RIXS spectra signifies a non-negligible electron-phonon coupling between valence electrons and the 7 meV phonon mode<sup>34-37</sup>. While we cannot fully rule out a small contribution of the P2 phonon mode (~12.9 meV or 3.13 THz) in the RIXS response, the coupling of valence-band electron to phonon is dominated by the 7 meV phonon mode. Distinct from this valence-band electron-phonon coupling scenario, CPS results have revealed that the P2 phonon mode dominates coupling to the above-gap electronic transition. Overall, the absence of a RIXS feature at ~3.13 THz supports our interpretation of the CPS data that points to an additional coupling mechanism beyond the common electron-phonon interaction associated with the valence band<sup>39,40</sup>, in which a photo-excited carrier or above-gap optical transition is absent.

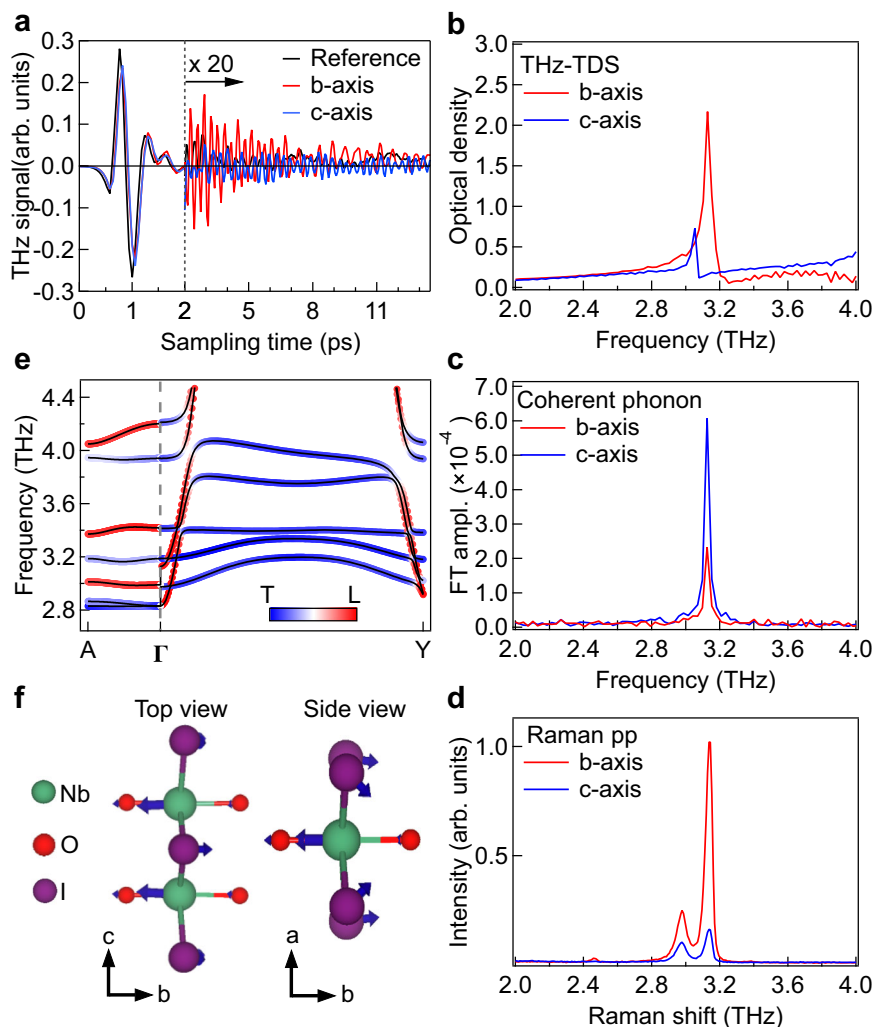


**Fig. 4 | Confirmation of the Ferroelectric TO mode.** **a, b** Polarization-dependent THz absorption spectra of a 2.6  $\mu\text{m}$  thick  $\text{NbOI}_2$  in **(a)** time domain and **(b)** frequency domain, respectively. The reference signal represents the THz signal without transmitting through the  $\text{NbOI}_2$  sample. The shoulder peak at  $3.044 \pm 0.023$  THz does not match the shoulder peak found in the Raman spectrum with its Raman shift being 2.98 THz. We assign the 3.04 THz mode to a different TO phonon with a relatively low Raman cross-section which is nonetheless IR active. **c** FT spectra of the oscillatory component at exciton-resonant region obtained from CPS. **d** Co-polarized Raman spectra of  $\text{NbOI}_2$  with off-resonant pump. **e** Calculated phonon dispersion based on first-principles DFT calculation with selected  $\mathbf{q}$  directions. Here, **A** denotes a vector perpendicular to the crystallographic  $bc$ -plane, whereas **Y** denotes a vector parallel to the

crystallographic  $b$ -axis. Color contrast represents different levels of transverse or longitudinal character. An additional phonon dispersion considering the vdW correction was performed and shown in Supplementary Fig. 11, which shows negligible difference from the current result. Supplementary Files include  $\text{NbOI}_2$  primitive cells optimized by the functions with and without the vdW correction. **f** Atomic motions (represented as blue arrows) of the TO phonon mode at 2.830 THz (calculated frequency of the P2 mode) viewed perpendicular to crystallographic  $bc$ -plane (top view) and along the  $c$ -axis (side view). Note that for graphing clarity, the length of the eigenvectors shown as arrows here do not represent the relative amplitude. The ratio of the relative amplitude of the eigenvectors for Nb and O ( $l_{\text{Nb}}/l_{\text{O}}$ ) is  $\sim 3.9$ .

In summary, we present experimental evidence for the dominant coupling of the above-gap electronic transition to a phonon mode at 3.1 THz in the 2D ferroelectric semiconductor  $\text{NbOI}_2$ . This mode is identified as the TO phonon mode, uniquely linked to the ferroelectric polarization, by Raman spectroscopy, pump-probe coherent spectroscopy, THz-TDS, and first principles calculation. Our findings provide direct evidence for the importance of specific forms of electron-TO phonon coupling in a 2D ferroelectric semiconductor. This is distinct from the well-known electron coupling to LO phonons in conventional semiconductors described by the Fröhlich model. The observed coupling to the TO phonon is specific to electronic excitation above the semiconductor bandgap and is absent for the valence band probed by RIXS spectroscopy.

Our finding reveals the distinct coupling of the above-gap electronic transition and associated photo-carriers to ferroelectric

polarization through the soft TO phonon mode. While this type of coupling has been proposed for a range of paraelectric materials<sup>5–9</sup>, invoked in the ferroelectric polaron model for LHPs<sup>10–13</sup> and  $\text{Bi}_2\text{O}_2\text{Se}$ <sup>14</sup>, and suggested for the ferroelectric semiconductor  $\text{SbSI}$ <sup>17</sup>, the unambiguous results presented here experimentally confirm the proposed charge carrier-TO phonon coupling. We believe this type of carrier-TO phonon coupling is of general importance for the efficient screening of the Coulomb potential and, thus, serving as a guiding principle in the search of defect tolerant semiconductors for optoelectronics from displacive ferro- or para-electric materials. Further, this coupling suggests a promising platform for realizing ultrafast modulation of polarization amplitude under sub-picosecond through optical excitation. Distinct from polarization switching enabled by strong THz field<sup>41</sup>, a pulse with visible-light frequency can launch ferroelectric TO phonon via the coupling we found. We suggest that this finding not

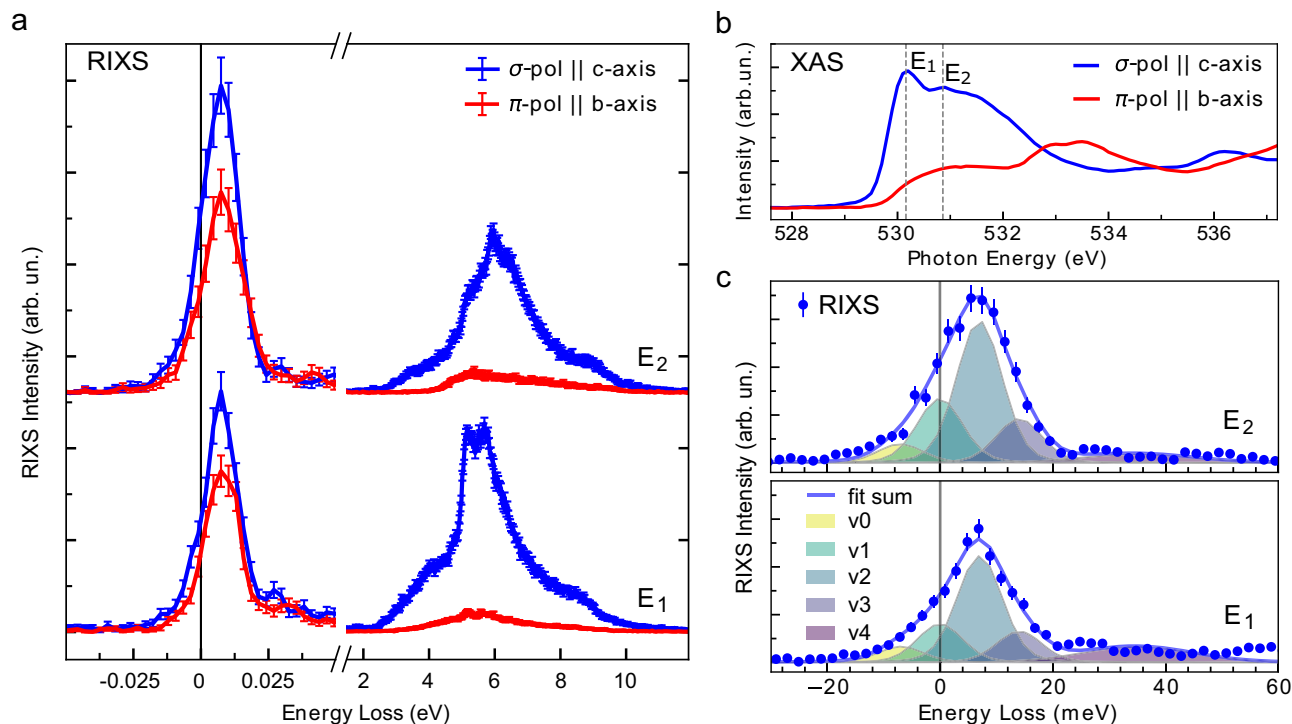


**Fig. 5 | Resonant Inelastic X-ray Scattering (RIXS) Reveals Electron-Phonon Coupling in the Valence Band.** **a** RIXS spectra measured at the O-K edge, with  $\sigma$  (blue) and  $\pi$  (red) polarized light at  $T = 35\text{K}$ . The incident photon energies were selected according to the main peaks displayed by the O-K XAS, shown in **(b)**. **c** Low-energy zoom-in of the RIXS spectra, measured for  $\sigma$  polarization (blue dots) at various incident photon energies. The spectra were fitted with five Voigt-shaped

functions respectively centered at  $-7\text{ meV}$  ( $v_0$ ),  $0\text{ meV}$  ( $v_1$ ),  $7\text{ meV}$  ( $v_2$ ),  $14\text{ meV}$  ( $v_3$ ), and  $36\text{ meV}$  ( $v_4$ ). The first four peaks are resolution-limited. The fit sum is represented by the blue solid line. Error bars indicate one standard deviation. Similar results are obtained for  $\pi$  polarization, see Supplementary Fig. 12. RIXS spectra showing full range of energy loss were also shown in Supplementary Fig. 12.

only is of importance to understanding the electronic properties of 2D ferroelectric semiconductors but also shed light on the future development of ferroelectric devices with tunable polarization fields.

## Methods

### Polarization-angle resolved Raman spectroscopy

The low-frequency Raman scattering measurements were carried on a home-built setup with a Nikon TE-300 inverted microscopy. A 633 nm HeNe laser first passed a linear polarizer and was filtered by a reflective band-rejection filter (Ondax), then sent through a half wave plate to control the angle of the incident polarization, and into the microscope objective (40X, NA = 0.6). The incident light was focused on a cleaved NbOI<sub>2</sub> single crystal mounted on a Si/SiO<sub>2</sub> wafer secured in a vacuum environment (Oxford MicroStat Hi-Res2). The Raman scattered light was collected through the same objective and the same half-wave plate, which projects the co-polarized Raman signal onto the polarization axis at the incident laser and the cross-polarized Raman signal onto the orthogonal axis. Then, the Raman scattered signal was sent through two-notch filters to filter out the Rayleigh scattered laser line. The Raman signal was focused onto the entrance slit of a spectrometer (Princeton Instruments HRS-300) with a 2400 gr/mm holographic grating that dispersed the spectrum onto a LN<sub>2</sub> cooled CCD camera (Princeton Instruments LN400/B). The Raman shift was calibrated by a dual Hg/He atomic emission lamp.

### Polarization-angle resolved reflection spectroscopy

Broadband tungsten-halogen lamp was used for the light source. The broadband light was sent through a linear polarizer followed with a half-wave plate to control the incident polarization. The polarized incident light was reflected to a 50:50 beam splitter with a small incident angle and then sent through the same microscope used for polarization-angle resolved Raman spectroscopy and focused on an

exfoliated few-layer NbOI<sub>2</sub> on a z-cut quartz substrate with the microscope objective (40X, NA = 0.6). The reflected white light was sent back through the same objective and beam splitter and was focused on the same spectrometer used for polarization-angle resolved Raman spectroscopy with a 150 gr/mm grating. The sample was measured under air.

### Coherent phonon spectroscopy

The pump and probe beams were derived from the fundamental output of an ultrafast Ti:sapphire regenerative amplifier (Coherent Legend) operating at a 10 kHz repetition rate. The pump beam was converted to 480 nm (40  $\mu\text{W}$ ) by a home-built noncollinear optical parametric amplifier (NOPA) and mechanically chopped at 5 kHz to match the second resonant energy of NbOI<sub>2</sub> along the *c*-axis, while the probe beam was a broadband white light spanning 470–870 nm generated from a *c*-cut sapphire plate. Due to scattering from pump light, the reflectance signal from probe light at  $480 \pm 10\text{ nm}$  was excluded. The polarization of the incident pump and probe beams was controlled by half-wave plates, with an additional linear polarizer used for the probe beam. The two beams overlapped at a nearly normal incidence on an NbOI<sub>2</sub> crystal (the same crystal used for polarization-angle resolved Raman spectroscopy) mounted on a Si/SiO<sub>2</sub> wafer in a nitrogen gas-tight cell. The reflected probe beam is then dispersed by a 600 gr/mm diffraction grating blazed at 500 nm and focused on a line-scan CCD camera (e2v AViVA EM4). The beam spot diameter is  $\sim 100\ \mu\text{m}$ .

### Nanosecond-scale transient reflectance spectroscopy

Transient reflectance measurements were carried out by using the broadband pump-probe setup (Helios spectrometers, Ultrafast Systems). The pump beam of 470 nm was generated in a collinear optical parametric amplifier (OPerA Solo, Light conversion) pumped by the

800 nm output of an amplified Ti:Sapphire laser (Coherent Astrella, 1 kHz). The probe light was generated by focusing the fundamentals of the Astrella laser system in a sapphire crystal. The pump-probe delay was controlled by a mechanical delay line. The two beams overlapped at a nearly normal incidence on an NbOI<sub>2</sub> crystal (the same crystal used for polarization-angle resolved Raman spectroscopy and coherent phonon spectroscopy) mounted on a Si/SiO<sub>2</sub> wafer in a nitrogen gas-tight cell. The beam spot diameter is ~1 mm.

### Scanning tunneling microscopy (STM)

STM measurements were performed on bulk crystals of NbOI<sub>2</sub> which were freshly cleaved in ultrahigh vacuum. Measurements were conducted at  $T=292$  K with an Omicron VT-STM using electrochemically etched tungsten tips that were calibrated on the surface of Cu (111) prior to each sample approach. Topographic images were collected in the constant current mode with a setpoint bias and current of 1 V, 50 pA.

### Terahertz time-domain spectroscopy (THz-TDS)

THz-TDS was performed based on the procedure described in ref. 42. Briefly, the output of Ti:sapphire regenerative amplifier (RA) with a pulse duration of 30 fs, a repetition rate of 10 kHz, and a wavelength centered at 800 nm (Coherent, Legend) was separated into two beams for THz generation and sampling. The THz probe was generated using the two-color air plasma method. The THz beam was collimated and then focused onto a NbOI<sub>2</sub> sample mounted on a 1 mm precision pinhole (Thorlabs) that defines the sample area having high homogeneity. Reference TDS was taken with another blank precision pinhole. The transmitted THz probe was collected and focused onto a 1 mm (110) ZnTe crystal. Another 800 nm sampling beam was directed onto ZnTe, by which the time-domain THz field was recorded via electro-optic sampling. The transmittance was obtained by dividing the sample and reference data after Fourier transformation. Prior to THz-TDS, the crystal orientation was first determined using in situ visible polarimetry equipped inside the THz setup. The THz setup was purged with dry air, and the measurements were performed at room temperature. For the NbOI<sub>2</sub> sample preparation for THz-TDS, a flake of NbOI<sub>2</sub> was cleaved from a bulk crystal with thermal release tape (TRT) and thinned with Scotch tape. The NbOI<sub>2</sub> thin flake was mounted to a pinhole with double-sided Kapton tape and heated to 135 °C to remove the TRT.

### First-principles calculation

The phonon and Raman spectra were simulated using first-principles density functional theory (DFT) calculations. We employed the Perdew-Burke-Ernzerhof (PBE) functional<sup>43</sup> for electronic structure and atomic position optimization, as implemented in the VASP package<sup>44,45</sup>. For calculation including the van der Waals correction, we employed PBE + D3 function for structure and atomic position optimization<sup>46</sup>. The simulation was conducted using the primitive cell of NbOI<sub>2</sub>, with a plane-wave basis cutoff of 500 eV. The Brillouin zone was sampled using a  $\Gamma$ -centered  $6 \times 6 \times 6$  k-point mesh. The force on each atom was converged to less than 0.0001 eV/Å. Phonon calculations were performed using the supercell frozen phonon approach, with structures generated by the Phonopy code<sup>47,48</sup> based on a  $3 \times 3 \times 3$  supercell. Non-analytic corrections for LO-TO splitting in polar materials were accounted for using Born effective charges<sup>33</sup>. The dielectric tensor and Born effective charges were calculated through density functional perturbation theory (DFPT)<sup>49</sup>. Raman tensors were subsequently derived using finite differences on the dielectric tensors<sup>50</sup>. For experimental comparison, phonon line widths were computed via the 3rd order force constants<sup>47,51</sup> and a supercell approach, involving 9240 displaced structures from a  $2 \times 2 \times 2$  supercell. The final angular-dependent Raman intensities included phonon linewidth at the  $\Gamma$  point at 300 K.

### X-ray absorption spectroscopy (XAS) and resonant inelastic X-ray scattering (RIXS)

The XAS and RIXS measurements were performed at the SIX 2-ID Beamline of NSLS-II<sup>52</sup>. The RIXS energy resolution was  $\Delta E = 13$  meV. The spectrometer was set to  $2\theta = 150^\circ$ , while the sample incident angle was  $\theta = 90^\circ$ . Under this experimental configuration, the  $\sigma$ -polarized incoming x-rays were parallel to the sample  $c$ -axis, while the  $\pi$ -polarized ones were parallel to the  $b$ -axis. The temperature was 35 K for all measurements. The NbOI<sub>2</sub> single crystal, aligned using the reflectance measurement, was glued by silver paint on a Cu-sample plate and cleaved in the air with Scotch tape just before loading it into the load lock chamber.

### Data availability

The data within this paper are available upon request. The structures of NbOI<sub>2</sub> primitive cells optimized by PBE and PBE + D3 functions are provided in the Supplementary Information files.

### References

- Fröhlich, H. Electrons in lattice fields. *Adv. Phys.* **3**, 325–361 (1954).
- Emin, D. *Polarons*. (Cambridge University Press, Cambridge, 2013).
- Scott, J. F. Soft-mode spectroscopy: Experimental studies of structural phase transitions. *Rev. Mod. Phys.* **46**, 83–128 (1974).
- Lines, M. E. & Glass, A. M. *Principles and Applications of Ferroelectrics and Related Materials*. (Oxford University Press, Oxford, 1977).
- Wemple, S. H., DiDomenico, M. & Jayaraman, A. Electron scattering in perovskite-oxide ferroelectric semiconductors. *Phys. Rev.* **180**, 547–556 (1969).
- Zhou, J.-J., Hellman, O. & Bernardi, M. Electron-phonon scattering in the presence of soft modes and electron mobility in SrTiO<sub>3</sub> perovskite from first principles. *Phys. Rev. Lett.* **121**, 226603 (2018).
- Imaseki, T. & Kinase, W. Electron-scattering model in perovskite oxide ferroelectric semiconductors. *Phys. Rev. B* **27**, 1228–1232 (1983).
- Zook, J. D. & Casselman, T. N. Electro-optic effects in paraelectric perovskites. *Phys. Rev. Lett.* **17**, 960 (1966).
- Nasu, K. Photogeneration of superparaelectric large polarons in dielectrics with soft anharmonic T<sub>1u</sub> phonons. *Phys. Rev. B Condens. Matter Mater. Phys.* **67**, 1–8 (2003).
- Miyata, K. & Zhu, X.-Y. Ferroelectric large polarons. *Nat. Mater.* **17**, 379–381 (2018).
- Wang, F. et al. Solvated electrons in solids—ferroelectric large polarons in lead halide perovskites. *J. Am. Chem. Soc.* **143**, 5–16 (2021).
- Fu, Y., Jin, S. & Zhu, X.-Y. Stereochemical expression of ns<sup>2</sup> electron pairs in metal halide perovskites. *Nat. Rev. Chem.* **5**, 838–852 (2021).
- Zhu, H. et al. Screening in crystalline liquids protects energetic carriers in hybrid perovskites. *Science* **353**, 1409–1413 (2016).
- Wang, F. et al. Phonon signatures for polaron formation in an anharmonic semiconductor. *Proc. Natl. Acad. Sci. USA* **119**, e2122436119 (2022).
- Ma, J., Yang, R. & Chen, H. A large modulation of electron-phonon coupling and an emergent superconducting dome in doped strong ferroelectrics. *Nat. Commun.* **12**, 2314 (2021).
- Yildirim, T. Ferroelectric soft phonons, charge density wave instability, and strong electron-phonon coupling in BiS<sub>2</sub> layered superconductors: A first-principles study. *Phys. Rev. B* **87**, 020506 (2013).
- Ziffer, M. E. et al. Charge carrier coupling to the soft phonon mode in a ferroelectric semiconductor. *Phys. Rev. Mater.* **6**, 095401 (2022).
- Abdelwahab, I. et al. Giant second-harmonic generation in ferroelectric NbOI<sub>2</sub>. *Nat. Photon.* **16**, 644–650 (2022).
- Wu, Y. et al. Data-driven discovery of high performance layered van der Waals piezoelectric NbOI<sub>2</sub>. *Nat. Commun.* **13**, 1884 (2022).

20. Fang, Y., Wang, F., Wang, R., Zhai, T. & Huang, F. 2D NbOI<sub>2</sub>: A Chiral Semiconductor with Highly In-Plane Anisotropic Electrical and Optical Properties. *Adv. Mater.* **33**, 2101505 (2021).
21. Werner, P. & Eckstein, M. Nonequilibrium resonant inelastic x-ray scattering study of an electron-phonon model. *Phys. Rev. B* **104**, 85155 (2021).
22. Ament, L. J. P., van Veenendaal, M., Devereaux, T. P., Hill, J. P. & van den Brink, J. Resonant inelastic x-ray scattering studies of elementary excitations. *Rev. Mod. Phys.* **83**, 705–767 (2011).
23. Yamagami, K. et al. Localized character of charge excitations for La<sub>2-x</sub>Sr<sub>x</sub>NiO<sub>4+δ</sub> revealed by oxygen K-edge resonant inelastic x-ray scattering. *Phys. Rev. B* **102**, 165145 (2020).
24. Ribeiro, H. B. et al. Unusual angular dependence of the raman response in black phosphorus. *ACS Nano* **9**, 4270–4276 (2015).
25. Peter, Y. U. & Cardona, M. *Fundamentals of Semiconductors: Physics and Materials Properties*. (Springer Science & Business Media, 2010).
26. Loudon, R. The Raman effect in crystals. *Adv. Phys.* **13**, 423–482 (1964).
27. Guo, Q. et al. Ultrathin quantum light source with van der Waals NbOCl<sub>2</sub> crystal. *Nature* **613**, 53 (2023).
28. Carbonnière, P., Erba, A., Richter, F., Dovesi, R. & Rérat, M. Calculation of anharmonic IR and Raman intensities for periodic systems from DFT calculations: Implementation and validation. *J. Chem. Theory Comput.* **16**, 3343–3351 (2020).
29. Cheng, T. K. et al. Impulsive excitation of coherent phonons observed in reflection in bismuth and antimony. *Appl. Phys. Lett.* **57**, 1004 (1990).
30. Zeiger, H. J. et al. Theory for displacive excitation of coherent phonons. *Phys. Rev. B* **45**, 768 (1992).
31. Thouin, F. et al. Phonon coherences reveal the polaronic character of excitons in two-dimensional lead halide perovskites. *Nat. Mater.* **18**, 349–356 (2019).
32. Park, M. et al. Excited-state vibrational dynamics toward the polaron in methylammonium lead iodide perovskite. *Nat. Commun.* **9**, 2525 (2018).
33. Gonze, X. & Lee, C. Dynamical matrices, Born effective charges, dielectric permittivity tensors, and interatomic force constants from density-functional perturbation theory. *Phys. Rev. B* **55**, 10355–10368 (1997).
34. Ament, L. J. P., van Veenendaal, M. & van den Brink, J. Determining the electron-phonon coupling strength from Resonant Inelastic X-ray Scattering at transition metal L-edges. *Europhys. Lett.* **95**, 27008 (2011).
35. Dashwood, C. D. et al. Probing electron-phonon interactions away from the Fermi level with resonant inelastic X-Ray scattering. *Phys. Rev. X* **11**, 41052 (2021).
36. Johnston, S. et al. Electron-lattice interactions strongly renormalize the charge-transfer energy in the spin-chain cuprate Li<sub>2</sub>CuO<sub>2</sub>. *Nat. Commun.* **7**, 10563 (2016).
37. Meyers, D. et al. Decoupling carrier concentration and electron-phonon coupling in oxide Heterostructures observed with resonant inelastic X-Ray scattering. *Phys. Rev. Lett.* **121**, 236802 (2018).
38. Olszta, M. J., Wang, J. & Dickey, E. C. Stoichiometry and valence measurements of niobium oxides using electron energy-loss spectroscopy. *J. Microsc.* **224**, 233–241 (2006).
39. Grüneis, A. et al. Electronic structure and electron-phonon coupling of doped graphene layers in  $\text{KC}_8$ . *Phys. Rev. B* **79**, 205106 (2009).
40. Pintschovius, L. Electron-phonon coupling effects explored by inelastic neutron scattering. *Phys. Status Solidi* **242**, 30–50 (2005).
41. Qi, T., Shin, Y.-H., Yeh, K.-L., Nelson, K. A. & Rappe, A. M. Collective coherent control: Synchronization of polarization in ferroelectric PbTiO<sub>3</sub> by shaped THz fields. *Phys. Rev. Lett.* **102** <https://doi.org/10.1103/PhysRevLett.102.247603> (2009).
42. Handa, T. et al. Spontaneous exciton dissociation in transition metal dichalcogenide monolayers. *Sci. Adv.* **10**, eadj4060 (2024).
43. Perdew, J. P., Burke, K. & Ernzerhof, M. Generalized Gradient Approximation Made Simple. *Phys. Rev. Lett.* **77**, 3865–3868 (1996).
44. Kresse, G. & Furthmüller, J. Efficiency of ab-initio total energy calculations for metals and semiconductors using a plane-wave basis set. *Comput. Mater. Sci.* **6**, 15–50 (1996).
45. Kresse, G. & Furthmüller, J. Efficient iterative schemes for ab initio total-energy calculations using a plane-wave basis set. *Phys. Rev. B* **54**, 11169–11186 (1996).
46. Grimme, S., Antony, J., Ehrlich, S. & Krieg, H. A consistent and accurate ab initio parametrization of density functional dispersion correction (DFT-D) for the 94 elements H-Pu. *J. Chem. Phys.* **132**, 154104 (2010).
47. Togo, A. First-principles Phonon Calculations with Phonopy and Phono3py. *J. Phys. Soc. Japan* **92**, 012001 (2022).
48. Togo, A., Chaput, L., Tadano, T. & Tanaka, I. Implementation strategies in phonopy and phono3py. *J. Phys. Condens. Matter* **35**, 353001 (2023).
49. Baroni, S., de Gironcoli, S., Dal Corso, A. & Giannozzi, P. Phonons and related crystal properties from density-functional perturbation theory. *Rev. Mod. Phys.* **73**, 515–562 (2001).
50. Skelton, J. M. et al. Lattice dynamics of the tin sulphides SnS<sub>2</sub>, SnS and Sn<sub>2</sub>S<sub>3</sub>: vibrational spectra and thermal transport. *Phys. Chem. Chem. Phys.* **19**, 12452–12465 (2017).
51. Togo, A., Chaput, L. & Tanaka, I. Distributions of phonon lifetimes in Brillouin zones. *Phys. Rev. B* **91**, 94306 (2015).
52. Dvorak, J., Jarrige, I., Bisogni, V., Coburn, S. & Leonhardt, W. Towards 10 meV resolution: The design of an ultrahigh resolution soft X-ray RIXS spectrometer. *Rev. Sci. Instrum.* **87**, 115109 (2016).

## Acknowledgements

The Raman and coherent phonon spectroscopy experiments are supported by the US Army Research Office, grant number W911NF-23-1-0056. The THz-TDS and DFT efforts are supported by the Materials Science and Engineering Research Center (MRSEC) through NSF grant DMR-2011738. Support by the Air Force Office of Scientific Research under award number FA9550-22-1-0389 is acknowledged for the STM imaging experiments. The RIXS experiments were supported by the Center on Programmable Quantum Materials, an Energy Frontier Research Center funded by the U.S. Department of Energy (DOE), under award number DE-SC0019443. This research used beamline 2-ID of NSLS-II, a US DOE Office of Science User Facility operated for the DOE Office of Science by Brookhaven National Laboratory under contract no. DE-SC0012704. C.-Y.H. is supported by the Taiwan-Columbia Fellowship funded by the Ministry of Education of Taiwan and Columbia University. M.Y.S was supported by the Gordon and Betty Moore Foundation, grant DOI 10.37807/gbmf12235.

## Author contributions

C.-Y.H., X.R., and X.-Y.Z. conceived this project. C.-Y.H. carried out optical measurements with assistance by T.H., Y.L., G.H., and M.S. C.-Y.H. and N.O. prepared the exfoliated samples. D.G.C. synthesized the crystals and performed PXRD under the supervision by X.R. T.H., carried out THz-TDS measurements. D.G.C. and C.-Y.H. built the high-temperature optical measurement setup. Z.-H.C. carried out theoretical calculations under the supervision by D.R.R. M.T. performed the STM under the supervision by A.P. Y.S. performed NIR reflectance measurements under the supervision by D.N.B. M.E.Z. proposed the material. C.A.O., J.P., and V.B. carried out the XAS and RIXS. The manuscript was prepared by C.-Y.H., D.G.C., Z.-H.C., V.B., D.R.R., X.R., and X.-Y.Z. in consultation with all other authors. All authors read and commented on the manuscript.

## Competing interests

The authors declare no competing interests.

## Additional information

**Supplementary information** The online version contains supplementary material available at <https://doi.org/10.1038/s41467-025-57061-9>.

**Correspondence** and requests for materials should be addressed to David R. Reichman, Xavier Roy or Xiaoyang Zhu.

**Peer review information** *Nature Communications* thanks Tianyou Zhai, and the other anonymous reviewer(s) for their contribution to the peer review of this work. A peer review file is available.

**Reprints and permissions information** is available at <http://www.nature.com/reprints>

**Publisher's note** Springer Nature remains neutral with regard to jurisdictional claims in published maps and institutional affiliations.

**Open Access** This article is licensed under a Creative Commons Attribution-NonCommercial-NoDerivatives 4.0 International License, which permits any non-commercial use, sharing, distribution and reproduction in any medium or format, as long as you give appropriate credit to the original author(s) and the source, provide a link to the Creative Commons licence, and indicate if you modified the licensed material. You do not have permission under this licence to share adapted material derived from this article or parts of it. The images or other third party material in this article are included in the article's Creative Commons licence, unless indicated otherwise in a credit line to the material. If material is not included in the article's Creative Commons licence and your intended use is not permitted by statutory regulation or exceeds the permitted use, you will need to obtain permission directly from the copyright holder. To view a copy of this licence, visit <http://creativecommons.org/licenses/by-nc-nd/4.0/>.

© The Author(s) 2025